# Second Generation Al$^{18}$F-labeled D-Amino Acid Peptide For CXCR4 Targeted Molecular Imaging

Muriel Aline Spahn[1*], Kaat Luyten[1*], Tom Van Loy[2], Mike Sathekge[3], Christophe M. Deroose[4], Michel Koole[4], Dominique Schols[2], Wim Vanduffel[5], Guy Bormans[1] and Frederik Cleeren[1**]

[1]*Laboratory for Radiopharmaceutical Research, Department of Pharmaceutical and Pharmacological Sciences, KU Leuven; Leuven, Belgium*
[2]*KU Leuven, Department of Microbiology, Immunology and Transplantation, Rega Institute for Medical Research, Laboratory of Virology and Chemotherapy, B-3000 Leuven, Belgium*
[3]*Department of Nuclear Medicine, University of Pretoria & Steve Biko Academic Hospital, Pretoria, South Africa*
[4]*Nuclear Medicine and Molecular Imaging, Department of Imaging and Pathology, KU Leuven; Leuven, Belgium*
[5]*Laboratory for Neuro- and Psychophysiology, KU Leuven Medical School, Leuven, Belgium*
*Contributed equally to this work
** Corresponding author

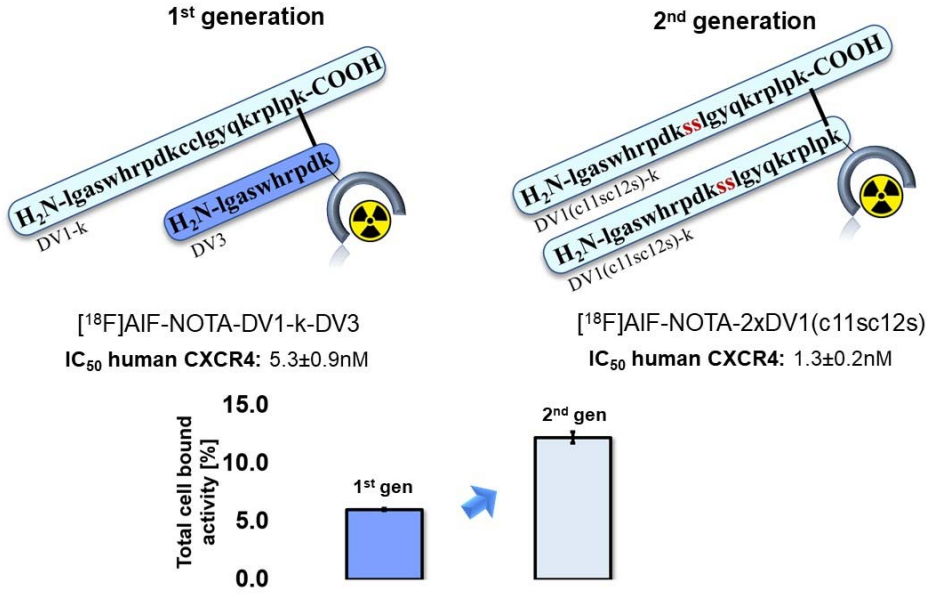


**Abstract**

Background: The C-X-C chemokine receptor type 4 (CXCR4) is overexpressed in many cancers, e.g. multiple myeloma and acute leukemia, yet solely [$^{68}$Ga]PentixaFor is used for clinical PET imaging. The aim of this study was to develop and assess a second generation Al$^{18}$F-labeled D-amino acid peptide based on the viral macrophage inflammatory protein II for CXCR4 targeted molecular imaging.

Methods: We designed a library of monomer and multimer constructs and evaluated their binding affinity for human and mouse CXCR4. Based on these results, we selected the best vector molecule for development of an Al$^{18}$F-labeled ligand, [$^{18}$F]AlF-NOTA-2xDV1(c11sc12s), which was further evaluated in a cell-based binding assay to assess its binding properties and specificity for CXCR4. Next, pharmacokinetics and tumor uptake of [$^{18}$F]AlF-NOTA-2xDV1(c11sc12s) were evaluated in naïve mice

and mice with xenografts derived from U87.CXCR4 cells. Finally, we performed an imaging study in a non-human primate to assess the *in vivo* distribution of this novel radioligand in a species closely related to humans.

Results: The lead ligand AlF-NOTA-2xDV1(c11sc12s) showed six-fold higher affinity for human CXCR4 compared to Ga-Pentixafor. The corresponding radiotracer was obtained in a good radiochemical yield of 41.1 ± 15.5% (n = 3) and apparent molar activity of 19.6 ± 3.5 MBq/nmol (n = 3) after optimization. In U87.CD4.CXCR4 cell binding assays, the total bound fraction of [$^{18}$F]AlF-NOTA-(2x)DV1(c11sc12s) was 32.4 ± 1.8%. This fraction could be reduced by 82.5% in the presence of 75 µM AMD3100. In naïve mice, [$^{18}$F]AlF-NOTA-2xDV1(c11sc12s) accumulated in organs expressing mouse CXCR4, e.g. the liver ($SUV_{mean}$ (mean standardized uptake value) 75 min p.i. 11.7±0.6), which was blockable by co-injecting AMD3100 (5 mg/kg). In U87.CXCR4 xenografted tumor mice, the tumor uptake of [$^{18}$F]AlF-NOTA-2xDV1(c11sc12s) remained low ($SUV_{mean}$ 0.5±0.1), but was reduced by co-administration of AMD3100. Surprisingly, [$^{18}$F]AlF-NOTA-2xDV1(c11sc12s) exhibited a similar biodistribution in a non-human primate as in mice indicating off-target binding of [$^{18}$F]AlF-NOTA-2xDV1(c11sc12s) in liver tissue.

Conclusion: The second generation D-peptide based [$^{18}$F]AlF-NOTA-2xDV1(c11sc12s) does bind to CXCR4, however, the collected data sets suggest that there is at least one additional unidentified receptor involved in the binding of this radiotracer. Further optimization is required to allow future CXCR4-specific imaging applications.

## 1. Introduction

C-X-C chemokine receptor 4 (CXCR4) is part of the G protein-coupled receptor (GPCR) super family and is involved in a plethora of signaling pathways in cancer, which promote cell proliferation, angiogenesis, metastasis and create a beneficial microenvironment for the survival of cancerous cells [1]. A wide range of cancers overexpress CXCR4, including localized cancers such as breast, glioma or prostate cancer, but also systemic cancers, like multiple myeloma, chronic lymphocytic leukemia and Non-Hodgkin lymphoma [2]. Furthermore, CXCR4 expression has been associated with tumor recurrence, metastasis and survival in colorectal cancer [3, 4].

The CXCR4-targeting theranostic pair developed by Gourni et al. [2] with [$^{68}$Ga]PentixaFor (cyclo(D-Tyr$^1$-D-[NMe]Orn$^2$(AMBS-[$^{68}$Ga]DOTA)-Arg$^3$-Nal$^4$-Gly$^5$) used for positron emission tomography (PET) and [$^{90}$Y]/[$^{177}$Lu]PentixaTher, the 3-iodo-D-Tyr derivative of [$^{68}$Ga]PentixaFor, as the therapeutic counterpart, has shown that CXCR4 is a promising target for theranostic nuclear medicine applications [5]. The imaging probe [$^{68}$Ga]PentixaFor displays an excellent profile for visualization of hematological malignancies, however, the radionuclide gallium-68 exerts less favorable physical properties than

fluorine-18. Characteristics, like the half-life ($^{68}$Ga: 67.7 min vs. $^{18}$F: 109.7 min), production route ($^{68}$Ga via $Ge^{68}/Ga^{68}$ generator vs. $^{18}$F via cyclotron) and maximum energy of the emitted positron ($^{68}$Ga: 1.89 MeV vs. $^{18}$F: 0.63 MeV), makes fluorine-18 the PET radionuclide of choice, mainly due to logistical advantages. Indeed, high scale productions in hospitals with cyclotrons and the facile distribution to nearby centers is feasible [6] [7]. However, larger amounts of gallium-68 can also be obtained by proton irradiation of zinc-68 targets in a cyclotron, but this production method is not widely used yet [8].

With this in mind, the development of a fluorine-18 based [$^{68}$Ga]PentixaFor probe was attempted by derivatizing the cyclic peptide with a NODA or NOTA chelator allowing Al$^{18}$F-labeling. However, the modifications resulted in a decreased CXCR4 affinity or an unfavorable biodistribution profile, respectively [3]. Disparities in the binding profile of [$^{68}$Ga]PentixaFor derivatives most likely stem from the scaffold structure itself, which is entirely submerged in the CXCR4 receptor binding crevice, thus not allowing any further alterations [3]. A similar trend was mirrored in the binding and biodistribution profile of the therapeutic counterpart PentixaTher, where $Tyr^{I}$ is iodinated to increase the binding affinity. Compared to [$^{68}$Ga]PentixaFor, [$^{177}$Lu]PentixaTher showed elevated blood pool activity and elevated hepatic activity levels up to seven days p.i. in humans. Despite these shortcomings, [$^{177}$Lu]PentixaTher is currently the most promising CXCR4 targeting radiopharmaceutical, since it showed tumor remission in patients with hematological neoplasms, but there is still room for improvement regarding biodistribution, pharmacokinetics and dosimetry profile [5], [9], [10].

A promising platform for the development of novel anti-CXCR4 radioprobes is based on the viral macrophage-inflammatory protein-II (vMIP-II), a chemokine expressed by the human herpesvirus-8 that gained increasingly attention due to its ability to prevent the human immunodeficiency virus (HIV) from entering host cells by antagonizing CCR3, CCR5 and CXCR4 [11]. Many truncated derivatives from its 71 amino acid long scaffold have been reported that act as specific short-sequenced CXCR4 antagonists, when tested in 12G5 competitive assays [10–12]. V1 and V3 represent the first 21 or 10 amino acids of vMIP-II, respectively, and are named DV1 or DV3 in case the amino acids are present in the D-configuration [12]. Crystallography studies disclosed their folded structure upon binding CXCR4 [13] and pharmacological studies further displayed V1's superior affinity towards CXCR4 over V3, as it contains eleven additional amino acids and interacts with more residues of CXCR4 [12]. The affinity was later potentiated by linking DV1 to DV3 via a newly introduced Lys, generating DV1-k-DV3 [15].

The DV1-k-DV3 platform was previously used by Luyten *et al.* for the development of a first generation Al$^{18}$F-labeled anti-CXCR4 radioprobe, called [$^{18}$F]AlF-NOTA-DV1-k-(DV3) [16]. Although the *in vitro* binding affinity to human CXCR4 (hCXCR4) of DV1-k-(DV3) derivatives and [$^{nat}$Ga]PentixaFor was similar, lower tumor uptake for [$^{18}$F]AlF-NOTA-DV1-k-(DV3) was observed with a slow wash-out

over time. It was hypothesized that the high binding affinity of the DV1-k-(DV3) scaffold to mouse CXCR4 (mCXCR4), compared to [$^{nat}$Ga]PentixaFor that merely lacks binding affinity for mCXCR4 [16], combined with high expression of CXCR4 in mouse liver resulted in a strong liver uptake. In consequence, only a small fraction was able to reach the xenografted tumor over-expressing hCXCR4 [16]. In addition, wash-out from the tumor in function of time might also be partially explained by the presence of two cysteines in the DV1 sequence, which are sensitive to oxidation *in vivo*. It was indeed shown that formation of the intramolecular S-S bond resulted in a loss of affinity for both hCXCR4 and mCXCR4 [16].

Based on these findings, we designed and developed second generation anti-CXCR4 D-peptide-based radiopharmaceuticals with increased CXCR4 affinity to improve the tumor uptake and retention. As it was reported by Zhou et al. that DV1(c11a) and DV1(c11ac12a) conserved their high binding affinity towards hCXCR4 [12], we substituted one or both cysteine residue(s) of DV1 in DV1-k-(DV3) with alanine or serine to prevent *in vivo* oxidation.

Given that the individual binding affinity of DV1 is 10-fold higher than DV3 (32 nM vs. 439 nM, respectively, [12]), we then generated dimer and trimer constructs of DV1(c11sc12s), as we hypothesized that multimer constructs of modified DV1 would display a higher binding affinity for CXCR4 than the DV1-k-(DV3) constructs.

*In vitro* binding affinity (half-maximal inhibitory concentration ($IC_{50}$)) towards human and mouse CXCR4 was determined for all novel monomer and multimer constructs. Based on these results, the best vector molecule for development of an Al$^{18}$F-labeled ligand, [$^{18}$F]AlF-NOTA-2xDV1(c11sc12s) was selected, which was then evaluated in a cell binding assay. Pharmacokinetics and tumor uptake of [$^{18}$F]AlF-NOTA-2xDV1(c11sc12s) were evaluated in naïve mice and mice xenografted with a U87.CXCR4 tumor. Finally, we performed an imaging study in a non-human primate to assess the *in vivo* distribution of this novel radioligand in a species closely related to humans.

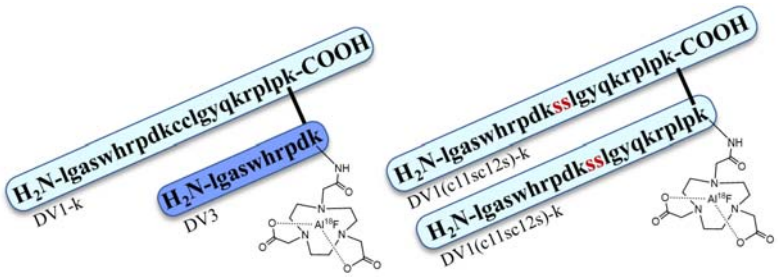


**Figure 1: Schematic structure of the first generation ligand [$^{18}$F]AlF-NOTA-DV1-k-(DV3) (left) and the second generation ligand [$^{18}$F]AlF-NOTA-2xDV1(c11sc12s) (right)**

## 2. Results & Discussion

### 2.1. *In vitro* assessment:

#### 2.1.1. CXCR4 affinity of DV probes

The first generation ligand, AlF-NOTA-DV1-k-(DV3), displayed a strong *in vitro* affinity towards hCXCR4 ($IC_{50}$ 5.3±0.9 nM) and mCXCR4 ($IC_{50}$ 33.4±13.5 nM), however, it showed only moderate *in vivo* hCXCR4 tumor uptake compared to [$^{68}$Ga]PentixaFor, with a slow wash-out over time [16]. Here, we hypothesized that forming a DV1 dimer might further improve the affinity, which might increase the *in vivo* CXCR4-specific tumor uptake. In addition, to prevent *in vivo* oxidation, one or both cysteine residues were substituted with amino acid residues sharing similar physicochemical characteristics, yet being resistant to *in vivo* oxidation. Both serine and alanine replaced the sulfhydryl-containing residues, as we hypothesized that this will most likely not interfere with the spatial configuration in the receptor fold. In total, we designed a library of nine new constructs and evaluated their binding affinities for hCXCR4 and mCXCR4. The $IC_{50}$-values in **Table 1** demonstrate that exchanging one cysteine residue with alanine or serine in DV1-k-(DV3) indeed did not affect binding affinity for hCXCR4. Substitution of both cysteine residues with alanine and serine in the DV1 sequence resulted however in a slight decrease in binding affinity.

***Table 1: $IC_{50}$ on Jurkat.hCXCR4 and U87.mCXCR4 cells.*** *All data are expressed as mean ± standard deviation (n=3).*

| Peptide | hCXCR4 $IC_{50}$ [nM] | mCXCR4 $IC_{50}$ [nM] |
|---|---|---|
| [$^{nat}$Ga]PentixaFor | 8.6 ± 1.1 [16] | > 1000 [16] |
| AMD3100 | 40.4 ± 3.5 [16] | 123.4 ± 17.0 [16] |
| AMD070 | 0.7 ± 0.1 | n.d. |
| DV1 | 241.7 ± 18.1 [16] | |
| DV3 | > 1000 [16] | |
| DV1-k-(DV3) | 2.9 ± 0.4 [16] | 41.5 ± 12.3 [16] |
| AlF-NOTA-DV1-k-DV3 | 5.3±0.9 [16] | 33.4±13.5 [16] |
| DV1(c11a)-k-(DV3) | 3.5 ± 0.7 | n.d. |
| DV1(c12a)-k-(DV3) | 2.6 ± 0.4 | |
| DV1(c11ac12a)-k-(DV3) | 20.1 ± 5.0 | |
| DV1(c11s)-k-(DV3) | 3.8 ± 0.5 | |
| DV1(c12s)-k-(DV3) | 2.7 ± 0.5 | |
| DV1(c11sc12s)-k-(DV3) | 16.0 ± 3.2 | |
| 2xDV1(c11sc12s) | 0.5 ± 0.2 | 6.9 ± 1.7 |
| 3xDV1(c11sc12s) | 0.2 ± 0.1 | 1.2 ± 0.5 |
| AlF-NOTA-2xDV1(c11sc12s) | 1.3 ± 0.2 | 7.2 ± 1.5 |

Based on previous findings of highly potent multimer constructs of DV1(c11a) [17] and DV3 [14], we also investigated the binding affinity of newly designed dimer and trimer constructs and their potential as vector molecules for molecular imaging. When comparing the binding affinity of DV1 and DV3 as such ($IC_{50}$ 241.7 nM ± 18.1 and $IC_{50}$ > 1000 nM, respectively), DV1 has a more than five-fold lower $IC_{50}$-value for hCXCR4 than DV3 and was therefore selected as building block for multimer constructs. To avoid *in vivo* disulfide bridge formation, both cysteine residues were substituted with a serine residue, as the serine-based sequence exhibited a slightly higher affinity than the alanine-based DV1 sequence ($IC_{50}$ 16.0 ± 3.2 nM and $IC_{50}$ 20.1 ± 5.0 nM, respectively). 2xDV1(c11sc12s) ($IC_{50}$ 0.5 ± 0.2 nM) displayed a significantly higher binding affinity for hCXCR4 than the original DV1-k-(DV3) ($IC_{50}$ 2.9 ± 0.4 nM) construct. The same drop in $IC_{50}$-value was observed for mCXCR4, when comparing 2xDV1(c11sc12s) ($IC_{50}$ 6.9 ± 1.7 nM) and DV1-k-(DV3) ($IC_{50}$ 41.5 ± 12.3 nM).

Our binding data are in line with the results of Choi *et al.* who demonstrated bivalent ligands containing two identical pharmacophores increase CXCR4 binding affinity for G protein-coupled receptor (GPCR) homodimers [17]. Molecular modeling revealed that a DV1 dimer can interact with a CXCR4 dimer by binding of their *N*-termini to both binding pockets of the CXCR4 dimer. This resulted in a two- to free-fold increase in antiviral activity and a 10-fold increase in binding affinity compared to its parent monomeric DV1 with less interactions with CXCR4 [17]. Furthermore, Lee *et al.* found that even a tetramer of DV3 had improved antiviral activity compared to its monomeric and dimeric construct [14]. We observed a similar trend for DV1(c11sc12s), for which the binding affinity of the trimer (3xDV1(c11sc12s)) increased compared to the dimeric construct 2xDV1(c11sc12s), with the increase in binding affinity being more pronounced for mCXCR4 (**Table 1**). The latter might be explained by inter species differences in receptor conformation.

Hence, the dimer of DV1(c11sc12s) was selected as vector molecule for further *in vitro* and *in vivo* evaluation based on the ease of synthesis and larger discrepancy between hCXCR4 and mCXCR4 affinity compared to 3xDV1(c11sc12s). The latter brings the advantage of preventing a pronounced bias in the biodistribution profile assessment stemming from mCXCR4 specific binding. 2xDV1(c11sc12s) was site-specifically derivatized with NOTA onto the ε-amino moiety of the *C*-terminal lysine of the second DV1 sequence and AlF-NOTA-2xDV1(c11sc12s) had a six-fold and four-fold higher binding affinity for hCXCR4 ($IC_{50}$ 1.3 ± 0.2 nM) than [$^{nat}$Ga]PentixaFor and AlF-NOTA-DV1-k-(DV3), respectively. The cross-reactivity of AlF-NOTA-2xDV1(c11sc12s) between hCXCR4 or mCXCR4 hints at a different binding profile and involved CXCR4 epitopes than the cyclic peptide [$^{nat}$Ga]PentixaFor, which did not show affinity for mCXCR4 ($IC_{50}$ >1000 nM) in our setup. Mouse and human CXCR4 share a sequence homology of 90.34% [18] and display a distinctively different extracellular loop 2 [19].

### 2.1.2. [$^{18}$F]AlF radiolabeling of NOTA-DV1-k-DV1(c11sc12s) and *in vitro* radiometabolite analysis

[$^{18}$F]AlF-NOTA-2xDV1(c11sc12s) was successfully produced by heating the reaction mixture at 100°C for 10 or 20 min, resulting in a decay-corrected RCY of 16 ± 3% (n = 11) or 41.1 ± 15.5% (n = 3), respectively. Both heating durations resulted in a radiochemical purity above 99% (n = 14). The apparent molar activity was 12.4 ± 3.9 MBq/nmol (n = 11) or 19.6 ± 3.5 MBq/nmol (n = 3), if the reaction mixture was heated for 10 or 20 min, respectively. Improving the RCY by prolonging the heating duration can be explained with the steric hindrance of the bulky structure of 2xDV1(c11sc12s), compared to DV1-k-(DV3) with 26 ± 6% (n = 6), which has 12 amino acids less. The production was performed in a cassette-based automated module and quality control was performed using radioHPLC using a polymer-based column. *In vitro* stability was confirmed in formulation buffer for 4.5 h at room temperature (**Figure S1**) and in human serum for 2 h at 37 °C (**Figure S1**). Respectively 96% and 95% of intact [$^{18}$F]AlF-NOTA-2xDV1(c11sc12s) was observed using radioHPLC, indicating excellent *in vitro* stability.

### 2.1.3. *In vitro* radioligand cell binding and internalization assay

[$^{18}$F]AlF-NOTA-2xDV1(c11sc12s) was first evaluated for *in vitro* specific binding to hCXCR4 in hCXCR4-overexpressing U87.CXCR4 cells, with or without co-incubation of AMD3100, AMD070 or 2xDV1(c11sc12s) at an inhibitor concentration of 100 µM (**Table 2**).

***Table 2 Total cell-bound fraction (membrane-bound + internalized fraction) of [$^{18}$F]AlF-NOTA-2xDV1(c11sc12s)*** *and the percentage of internalized ligand were determined using hCXCR4-expressing U87.CXCR4 cells (2.5×10$^5$ cells/well, 1 h at 37°C) in absence or presence of AMD3100 (100 µM), AMD070 (100 µM) or 2xDV1(c11sc12s) (100 µM). Compared to [$^{68}$Ga]PentixaFor and [$^{18}$F]AlF-NOTA-DV1-(DV3)* [16]. *Statistical analysis independent-samples t-test. All data are expressed as mean ± SD (n = 3). * p ≤ 0.01, ** p ≤ 0.001 (N.D.: not determined)*

| | **Total cell-bound fraction** [% of applied activity] | | | | **Internalized fraction** [% of total cell-bound fraction] |
|---|---|---|---|---|---|
| **Radiotracer** | | AMD3100 | AMD070 | 2xDV1(c11sc12s) | |
| [$^{68}$Ga]Pentixafor | 8.9 ± 0.3 | 0.1 ± 0.003* | n.d. | | 10.0 ± 0.1 |
| [$^{18}$F]AlF-NOTA-DV1-k-(DV3) | 6.0 ± 0.1 | 1.1 ± 0.1* | | | 20.1 ± 2.0 |
| [$^{18}$F]AlF-NOTA-2xDV1(c11sc12s) | 12.2 ± 0.5 | 1.1 ± 0.04** | 4.5 ± 1.0** | 0.1 ± 0.02** | 17.4 ± 0.4 |

Both AMD3100 and AMD070 are known CXCR4 antagonists, which differ in their pharmacokinetic properties, e.g. administration route of AMD3100 is mainly by i.v. injection, while AMD070 can also be orally administered [20]. The total-bound fraction of [$^{18}$F]AlF-NOTA-2xDV1(c11sc12s) is ~25% higher than [$^{68}$Ga]PentixaFor and increased ~two-fold compared to [$^{18}$F]AlF-NOTA-DV1-k-(DV3). Nonetheless, these findings suggest that the higher *in vitro* binding affinity of the DV1(c11sc12s) construct seems to contribute to the higher cell binding of [$^{18}$F]AlF-NOTA-2xDV1(c11sc12s). 17.4 ± 0.4% of the total cell-bound fraction of [$^{18}$F]AlF-NOTA-2xDV1(c11sc12s) was internalized. We did not

confirm if this is a result of uncomplete removal of the membrane-bound fraction during acidic washing steps or endocytosis of the radioligand-receptor complex. Although 2xDV1(c11sc12s) acts as a CXCR4 antagonist, we do not exclude endocytosis as Heon Lee *et al.* previously described the internalization of FITC-labeled 4xDV3 [14].

In addition, interesting results were obtained when co-incubating the radiotracer with an excess of CXCR4 antagonists. As for [$^{18}$F]AlF-NOTA-DV1-k-(DV3), co-incubation with AMD3100 did not result in a complete blockage (91% block observed) of [$^{18}$F]AlF-NOTA-2xDV1(c11sc12s) binding. This effect was even more distinct for AMD070, where only 63% of [$^{18}$F]AlF-NOTA-2xDV1(c11sc12s) was blocked. Considering the $IC_{50}$ of AMD070 being lower than the one of AMD3100 (Table 1), it was surprising to observe a lower blocking efficiency in the presence of AMD070. The deviation was hypothesized to stem from the different binding profiles with AMD3100 binding to the major binding pocket and AMD070 to the minor pocket [21]. Despite sharing similar amino acid residues for the receptor binding, like Asp$^{171}$, Glu$^{288}$, Trp$^{94}$ and Asp$^{262}$ [22]–[24], it was revealed that AMD3100 displayed a selective dependency on Asp262$^{6.58}$, located on top of the transmembrane (TM) helix 6, while Asp97$^{2.63}$, located on top of TM helix 2, is pivotal for AMD070 [21].

However, co-incubation with the vector molecule itself, (self-block), resulted in >98% blocking of [$^{18}$F]AlF-NOTA-2xDV1(c11sc12s) binding. Different factors can play a role in the differences found in blocking efficiency of AMD3100 or AMD070 vs. 2xDV1(c11sc12s). A possible explanation may be that the concentration of the antagonists is not high enough to compete with [$^{18}$F]AlF-NOTA-2xDV1(c11sc12s) which has a higher affinity for hCXCR4, although complete blocking of [$^{68}$Ga]PentixaFor cell binding with AMD3100 is possible. Secondly, [$^{18}$F]AlF-NOTA-2xDV1(c11sc12s) may (also) specifically bind to another target or epitope of CXCR4 than AMD3100 or AMD070.

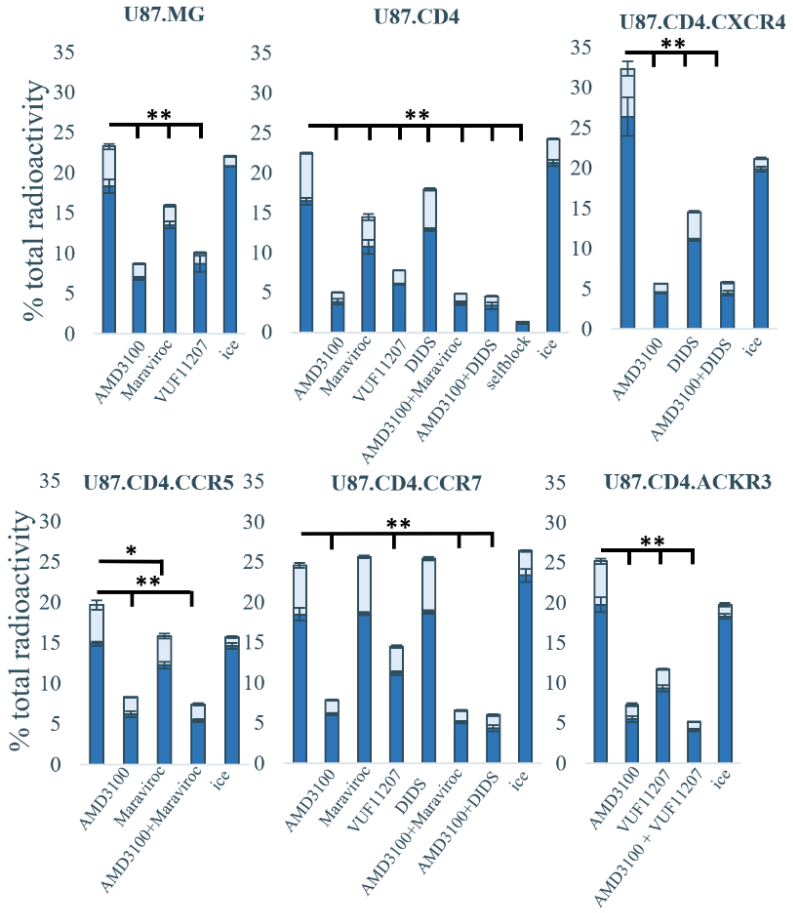


**Figure 2: Binding profile of [$^{18}$F]AlF-NOTA-2xDV1(c11sc12s) on U87 cells in the absence or presence of competitors at 37°C or on ice .** *The light blue bar stands for the internalized fraction and the dark blue for the membrane bound fraction. AMD3100 (CXCR4 antagonsist), Maraviroc (CCR5 antagonist), VUF11207 (ACKR3 chemokine receptor agonist), DIDS = 4,4'-diisothiocyanatostilbene-2,2'-disulfonic acid (inhibitor of cellular anion permeability) or (2x)DV1(c11sc12s) as self-block. The values are expressed as mean±SD (n=3). * $p < 0.05$, ** $p \leq 0.001$.*

To assess the CXCR4 specificity of [$^{18}$F]AlF-NOTA-2xDV1(c11sc12s), cell binding experiments have been performed in control U87 cells and U87 cells overexpressing CD4, CD4.CXCR4, CD4.CCR5, CD4.CCR7, or CD4. ACKR3. The results are shown in **Figure 2**. Of note, for clarity in the manuscript we report these results in this section, but this second set of cell binding experiments has been performed to further assess the CXCR4 specificity after we conducted the *in vivo* assessment in tumor mice and non-human primate. The highest cell binding (32.4 ± 1.8%) was observed in the U87.CD4.CXCR4 cells, indicating at least partial specific CXCR4 binding, however, the binding was not fully blockable using AMD3100 (75µM), resulting in 5.6 ± 0.1% remaining cell-bound activity and a block of 82.7%. This was somewhat lower but still comparable to the 91% blocking observed using the U87.CXCR4 cells using 100 µM AMD3100 (**Table 2**). This non quantitative blocking does not automatically imply

unspecific uptake, since AMD3100 binds to different CXCR4 epitopes, leaving the *N* terminus available for the radiotracer to bind and further, AMD3100 has a higher $IC_{50}$ compared to AlF-NOTA-2xDV1(c11sc12s) towards hCXCR4. Lowering the temperature to 4°C during the binding assays decreased the internalized fraction, which indicates that the tracer is at least partially actively endocytosed, although the total internalized fraction is limited.

It was surprising that cells missing CXCR4 expression on the cellular membrane still displayed substantial and blockable binding, suggesting a lack of selectivity for CXCR4. This hypothesis is further fueled by the observations made on U87.CXCR4 cells missing the CD4 overexpression (**Table 2**), where the radiotracer uptake was lower, despite CD4 not playing a fundamental role in the binding, and seemingly entirely blockable by adding ADM3100. Considering the homogenously increased total specific cell binding in the different U87 cell lines prompts the hypothesis, that the identity of the off-target protein(s) in question remains elusive. The selfblock U87.CD4 cells showed that the uptake of the radiotracer is specific to a certain target besides CXCR4, since the uptake is blockable up to 93%.

The recently published U87.MG surfaceome [25] gave additional insight on the presence of various different receptors, which might be involved in the binding of the radiotracer. However, assessing the binding profile of the radiotracer on other prevalent receptors or members associated with the CXCR or CCR family was limited due to the availability of cell lines specifically overexpressing one certain receptor, as well as specific competitors.

Taking into account the blocking studies, it might seem counter-intuitive that receptor-specific small molecules were able to decrease the cellular uptake on cells missing the overexpression of a certain CXCR or CCR, especially AMD3100. Hatse et al. [26] extensively assessed AMD3100's specificity on the receptors CXCR1 through CXCR3 and CCR1 through CCR9 and didn't observe any binding affinities. The receptor ACKR3 was skipped, since it was only discovered later, but Kalatskaya et al. [27] reported the recruitment of beta-arrestin by AMD3100 binding to ACKR3 via allosteric agonism. Gravel et al. [28] suggested the interaction of AMD3100 with ACKR3 is most likely attributed to the conserved amino acids Asp-171 and Asp-262 between CXCR4 and ACKR3, which are pivotal for the binding of AMD3100. Further the significance of assay parameters, e.g. cell line origin, applied temperature and concentration range, were underscored to have a distinctive impact on the selectivity profile of AMD3100. This in mind, one could argue that minor unspecific binding might have occurred, since the assays performed by Hatse et al. [26] mainly focused on $Ca^{2+}$ flux assays with strongly deviating assay settings. Though, this hypothesis warrants further examination for confirmation.

No similarly extensive binding studies have been conducted for the other small molecules, however, Maraviroc has been exposed to the heterodimer MOR-CCR5 on human astrocytes during a luciferase-

based HIV-$1_{SF162}$ infection assay and its affinity was diminished [29]. Whether this observation holds true for other receptors warrants further clarification. VUF11207 has solely been analyzed in a [$^{125}$I]I-CXCL12 radioligand binding assay [30], leaving ground to speculate over its receptor specificity.
Comparing these *in vitro* results with those from the first generation ligand DV1-k-DV3 on U87 cells overexpressing CXCR4, illustrated that the non-blockable percentage using AMD3100 is higher for the second generation tracer. This implies that replacing DV3 with DV1 might have further fueled the binding towards receptors other than CXCR4.

### 2.2. *In vivo* assessment:

#### 2.2.1. Biodistribution in wild-type mice

The *in vivo* biodistribution of [$^{18}$F]AlF-NOTA-2xDV1(c11sc12s) was first evaluated in wild-type mice. [$^{18}$F]AlF-NOTA-2xDV1(c11sc12s) displayed the same pharmacokinetic profile as [$^{18}$F]AlF-NOTA-DV1-k-(DV3) at 75 min p.i.. As shown in **Figure 3**, this includes accumulation in mCXCR4-expressing organs ($SUV_{liver}$ 11.7 ± 0.6, $SUV_{spleen}$ 3.6 ± 0.5, $SUV_{bone}$ 0.7 ± 0.1), high kidney accumulation and fast blood clearance. The expression of CXCR4, CCR5 and ACKR3 in murine whole liver has been confirmed via Western blot and is depicted in **Figure S2**. The degree of accumulation in the aforementioned organs correlates with the organ's perfusion rate, and is most pronounced in the liver and to a lesser extent in the spleen.

The enhanced binding affinity for mCXCR4 resulted in a significant increase of specific hepatic accumulation from SUV 7.4 ± 0.5 to 11.7 ± 0.6 ($p \leq 0.001$) for [$^{18}$F]AlF-NOTA-2xDV1(c11sc12s). Co-injection of 5 mg/kg AMD3100 displaced all CXCR4-specific binding ($SUV_{liver}$ 0.6, $SUV_{spleen}$ 0.2, $SUV_{bone}$ 0.2), which resulted in an increased [$^{18}$F]AlF-NOTA-2xDV1(c11sc12s) blood concentration and kidney accumulation. However, based on the *in vitro* cell binding data, the high liver accumulation and retention might also be non-CXCR4 specific binding that can still be displaced with AMD3100, but the mechanism or specic target responsible for this effect is not clear.
As previously discussed for [$^{18}$F]AlF-NOTA-DV1-k-(DV3), the high kidney accumulation of [$^{18}$F]AlF-NOTA-2xDV1(c11sc12s) may result from peptide reabsorption in the proximal tubular epithelial cells of the kidneys by the megalin-cubulin transporters.

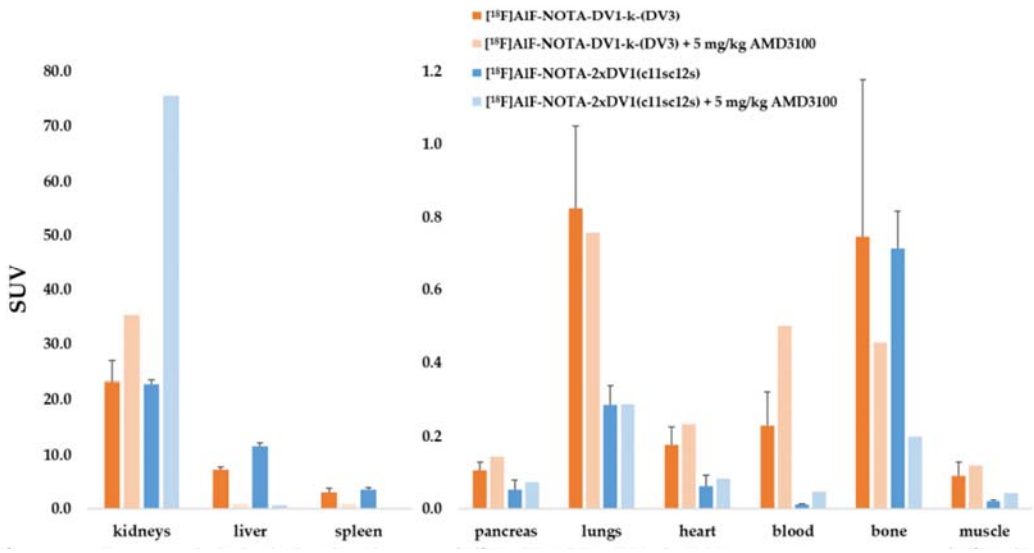


**Figure 3: *Ex vivo* biodistribution of [$^{18}$F]AlF-NOTA-DV1-k-DV3 (n=5) and [$^{18}$F]AlF-NOTA-2xDV1(c11sc12s) (n=4) in wild-type mice *75 min post-injection (p.i.)*** *with and without co-injection of AMD3100 (5mg/kg, n = 2 or 1 for [$^{18}$F]AlF-NOTA-DV1-k-DV3 or [$^{18}$F]AlF-NOTA-2xDV1(c11sc12s), respectively), data is expressed as standardized uptake values (SUV). Values are shown as mean ± SD.*

Plasma was analyzed for radiometabolites of [$^{18}$F]AlF-NOTA-2xDV1(c11sc12s) at 15 min or 75 min p.i. (**Figure S3**), and in urine at 75 min p.i. (**Figure S3**). After 15 min, 74 ± 7% ($n$ = 3) of the activity in plasma corresponded to [$^{18}$F]AlF-NOTA-2xDV1(c11sc12s), and this value was 70 ± 5% ($n$ = 3) at 75 min p.i.. In comparison to [$^{18}$F]AlF-NOTA-DV1-k-(DV3), the amount of intact radioligand was 10% lower in plasma at 15 and 75 min p.i., respectively. A large fraction of radioactivity in urine was found to be polar radiometabolites (69 ± 1%, $n$ = 3), which was also observed for [$^{18}$F]AlF-NOTA-DV1-k-(DV3) (63 ± 2%). Although a larger fraction of radiometabolites was detected in urine, we hypothesize that radiometabolites are enriched in urine due to the more efficient tubular reabsorption of the parent radioligand compared to the polar radiometabolites, which results in high renal retention and limited excretion to the bladder. Therefore, the fraction of radiometabolites in plasma is more representative to assess the *in vivo* stability and it can be concluded that [$^{18}$F]AlF-NOTA-2xDV1(c11sc12s) shows a reasonably good stability *in vivo.* This was anticipated as the D-conformation peptides are not expected to be substrates for enzymatic degradation.

### 2.2.2. Biodistribution in U87.hCXCR4 xenografted tumor mice

The tumor accumulation and retention of [$^{18}$F]AlF-NOTA-2xDV1(c11sc12s) was determined in hCXCR4-expressing tumor-bearing mice by *ex vivo* biodistribution at 75 min p.i. (**Table 3**) and dynamic µPET studies up to 60 min p.i.. **Figure 4** shows maximum intensity projection (MIP) images at 60 min p.i. and time activity curves (TACs) are shown in **Figure 5**. Different blocking conditions were explored to improve our understanding of the behavior of [$^{18}$F]AlF-NOTA-2xDV1(c11sc12s) in tissues of interest. [$^{18}$F]AlF-NOTA-2xDV1(c11sc12s) displayed a similar *in vivo* pharmacokinetic profile in a

hCXCR4-tumor mouse model as [$^{18}$F]AlF-NOTA-DV1-k-(DV3): mCXCR4-specific uptake and retention in liver, spleen and femur harboring bone marrow, fast clearance from the circulation, high non-CXCR4 related kidney accumulation and low hCXCR4-specific tumor uptake [16]. Co-injection with all CXCR4 blocking agents led to a significant increase of kidney uptake. Data of *ex vivo* biodistribution were in accordance with μPET data.

***Table 3: Ex vivo biodistribution of [$^{18}$F]AlF-NOTA-2xDV1(c11sc12s)*** *(n = 8) in U87.hCXCR4 tumor-bearing mice 75 min p.i. (results expressed as SUV). [$^{18}$F]AlF-NOTA-2xDV1(c11sc12s) + 5 mg/kg AMD3100 (co-injection, n = 4), displacement experiment (15 min p.i.) with 5 mg/kg AMD3100 (n = 4), [$^{18}$F]AlF-NOTA-2xDV1(c11sc12s) + 5 mg/kg AMD070 (co-injection, n = 4) or [$^{18}$F]AlF-NOTA-2xDV1(c11sc12s) + 15 nmol 2xDV1(c11sc12s) (co-injection, n = 3). Statistical analysis independent samples t-test. All data are expressed as mean ± SD. * $p < 0.05$, ** $p \leq 0.01$, *** $p \leq 0.001$.*

| | | AMD3100 | | | |
|---|---|---|---|---|---|
| **Organ** | **Naive** | **Co-injection** | **Displacement** | **AMD070** | **2xDV1(c11sc12s)** |
| **Kidneys** | 16.58±1.98 | 60.01±0.85*** | 31.37±5.15* | 28.23±0.94*** | 48.46±1.78*** |
| **Liver** | 11.14±0.97 | 0.74±0.11*** | 7.87±0.20*** | 9.94±0.30** | 0.89±0.28*** |
| **Spleen** | 3.06±0.78 | 0.39±0.06*** | 1.44±0.32*** | 2.54±0.51 | 0.30±0.01*** |
| **Bone** | 0.53±0.12 | 0.23±0.03*** | 0.40±0.03* | 0.35±0.06** | 0.15±0.01*** |
| **Tumor** | 0.47±0.09 | 0.27±0.05*** | 0.30±0.03*** | 0.08±0.00*** | 0.42±0.16 |
| **Muscle** | 0.04 ± 0.02 | 0.05 ± 0.01 | 0.07 ± 0.02 | 0.02 ± 0.01 | 0.08±0.06 |
| **Blood** | 0.05 ± 0.02 | 0.10±0.03 | 0.13±0.04 | 0.02±0.00 | 0.15±0.12 |

The downside of [$^{18}$F]AlF-NOTA-2xDV1(c11sc12s) displaying a CXCR4 cross-reactivity between human and mice resulted in an elevated hepatic uptake due to the high mCXCR4 expression in mouse liver. We hypothesize that a large fraction of the radiotracer is trapped in the liver, leaving only a small fraction to potentially bind the xenografted tumor. We were, however, not able to confirm if the observed low tumor uptake is CXCR4 specific or not. Further, high expression of CXCR4 is not observed in human liver [31], therefore, evaluation of this novel class of CXCR4-targeting radiotracers in preclinical tumor models does not predict its clinical potential.

Co-injection of 5 mg/kg AMD3100 completely blocked uptake in liver, spleen and femur harboring bone marrow, while significantly increasing the kidney retention. Further, a 41.84% blocking efficiency in the tumor was observed. However, as overall tumor uptake is low, it is uncertain if it is indeed hCXCR4 specific binding. Surprisingly the self-block with non-radioactive 2xDV1(c11sc12s) yielded a comparable tumor uptake as the baseline condition (9.00% blocking efficiency), despite almost

completely blocking the uptake *in vitro* (**Table 2** and **Figure 2**). Based on the observed decreased hepatic uptake, it might be hypothesized that that the majority of the non-radioactive compound is trapped inside of the liver alike the radiotracer, thus diminishing the full blocking efficiency of 2xDV1(c11sc12s) in the xenografted tumor.

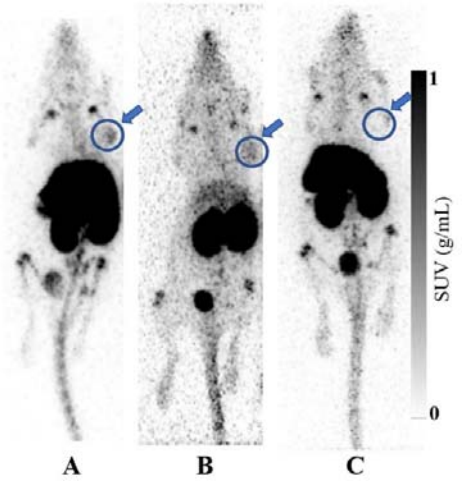


**Figure 4:** ***MIP images (60 min p.i.) of U87.hCXCR4 xenografted mice injected with [$^{18}$F]AlF-NOTA-2xDV1(c11sc12s)*** *(A, n = 8), or co-injected with 2xDV1(c11sc12s) (15 nmol) (B, n = 3), respectively. The displacement study with AMD3100 i.v. (5 mg/kg, n = 4) 15 min post [$^{18}$F]AlF-NOTA-2xDV1(c11sc12s) injection is shown in (C). The xenografted tumor has been circled and highlighted with an arrow.*

As we assumed that [$^{18}$F]AlF-NOTA-2xDV1(c11sc12s) binds in a reversible way to CXCR4, we expected a pronounced displacement effect in mCXCR4-expressing organs by i.v. injection of 5 mg/kg AMD3100 15 min after radioligand injection. Surprisingly, uptake in mCXCR4-expressing organs was only reduced by ~30%. This might hint at the different binding mechanisms, since the D-peptide might sterically hinder the access of the small molecule to the binding pockets located in the CXCR4 crevice. A recent study of Soave *et al.* revealed that binding of the CXCR4-targeting nanobody (Nb) VUN400 sterically hindered binding of AMD3100 to the receptor [32]. This may explain the limited displacement in mCXCR4-expressing organs with AMD3100. Furthermore, blocking with AMD070 only slightly reduced liver uptake in mouse with ~10% while it blocked binding to hCXCR4-expressing tumor cells *in vivo* with ~80%. The latter does not correspond with the incomplete blocking observed in cell binding experiments in U87.hCXCR4 cells. But also in this case, as overall tumor uptake is low, it is uncertain if it is indeed hCXCR4 specific binding.

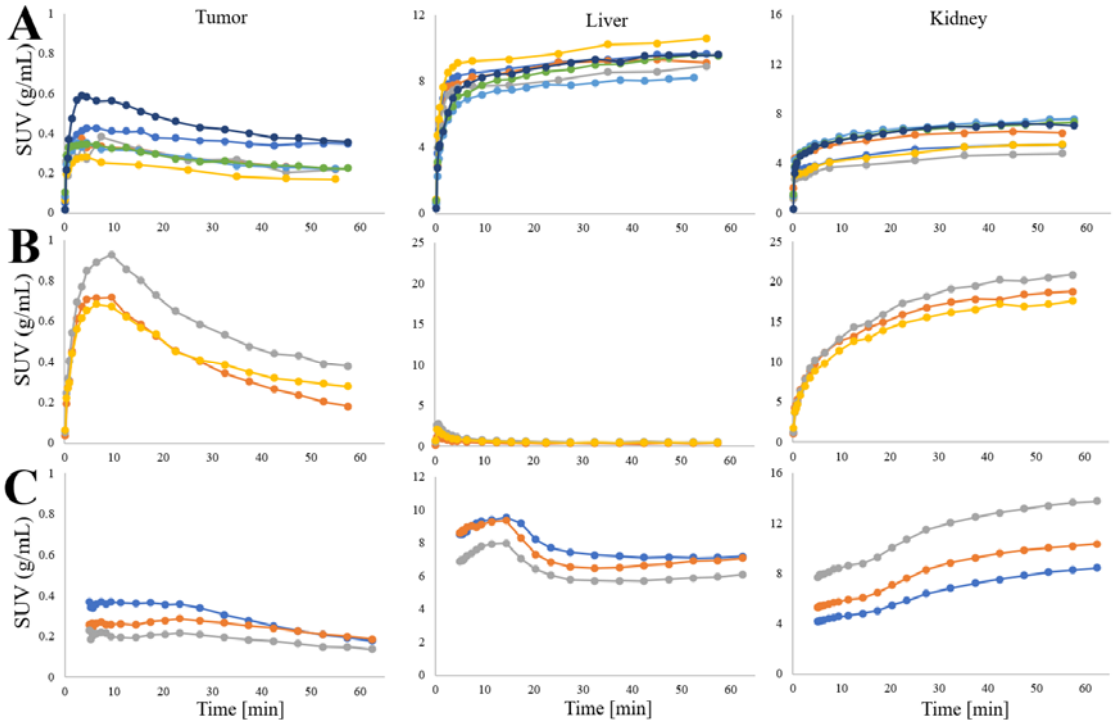


***Figure 5: TAC of U87.hCXCR4 xenografted mice injected with [$^{18}$F]AlF-NOTA-2xDV1(c11sc12s)*** *(A, n = 8) or co-injected with 2xDV1(c11sc12s) (B, n = 3 injected with 15 nmoles. The displacement study with AMD3100 (5mg/kg 15 min p.i.) has been added in (C, n =4) with the scan starting to acquire 5 min p.i. of [$^{18}$F]AlF-NOTA-2xDV1(c11sc12s).*

### 2.2.3. Biodistribution in a non-human primate

Since [$^{68}$Ga]PentixaFor is selective for hCXCR4, the dynamic biodistribution investigation of both CXCR4-targeting radioligand classes should be performed in a species representative for humans in order to allow a fair comparison of the performance of [$^{18}$F]AlF-NOTA-2xDV1(c11sc12s) vs. [$^{68}$Ga]PentixaFor. The sequence homology of hCXCR4 and CXCR4 of a rhesus macaque has been reported as 98.30% [18]. Further, in a clinical setting only limited uptake of [$^{68}$Ga]Pentixafor is observed in the liver ($SUV_{mean}$ = 1.46 50 min p.i.) [31]. Therefore, we performed a dynamic whole-body biodistribution of [$^{18}$F]AlF-NOTA-2xDV1(c11sc12s) in a non-human primate.

Surprisingly, [$^{18}$F]AlF-NOTA-2xDV1(c11sc12s) exhibited a similar biodistribution in a non-human primate as in mice, with a high uptake in the liver and spleen. Also uptake in the red bone marrow was observed (**Figure 6**). [$^{18}$F]AlF-NOTA-2xDV1(c11sc12s) accumulated in liver, reaching a plateau over time, while no hepatobiliairy clearance was observed. (**Figure 6C**). TACs obtained from mice exhibited the same uptake and excretion profile. In addition the uptake is blockable in mice and therefore we hypothesize that the hepatic accumulation is specific, but probably not CXCR4 specific, since the hepatic CXCR4 expression is expected to be similary low in non-human primates alike in humans. However, additional studies are needed to confirm the observed results and validate that liver uptake in

non-human primates is indeed due to off-target binding of [$^{18}$F]AlF-NOTA-2xDV1(c11sc12s). To confirm that uptake in these organs is CXCR4-specific, a blocking study with an excess of CXCR4 antagonist should be performed. Unfortunately, a blocking study requires high doses of CXCR4 inhibitor, which may result in unwanted side effects.

Furthermore, [$^{18}$F]AlF-NOTA-2xDV1(c11sc12s) displayed fast blood clearance and high accumulation in the kidney cortex (**Figure 6A**). The megalin-cubulin transporters in the proximal tubule are expected to reabsorb the peptide-based radioligand from the glomerular filtrate, resulting in a high renal radioactivity concentration. This is mirrored by the renal TAC (**Figure 6C**), which steadily increases over time, suggesting the radiotracer not being renally cleared.

Besides the biodistribution, we also quantified radiometabolites of [$^{18}$F]AlF-NOTA-2xDV1(c11sc12s) in non-human primate plasma 10 min (parent fraction: 97%), 30 min (96%) and 60 min (95%) p.i. during PET imaging. [$^{18}$F]AlF-NOTA-2xDV1(c11sc12s) displayed higher *in vivo* plasma stability in a non-human primate compared to mice (95% parent at 60 min p.i.in non-human primate vs. 70% at 75 min p.i. in mice, respectively), while the fraction of radiometabolites in urine was comparable though determined at different time points (32% at 180 min p.i. vs. 31% at 75 min p.i.). As plasma is the most representative for overall *in vivo* stability, we concluded that [$^{18}$F]AlF-NOTA-2xDV1(c11sc12s) is highly stable *in vivo* in a non-human primate. The corresponding radioHPLC chromatograms can be seen in **Figure S4-S5**.

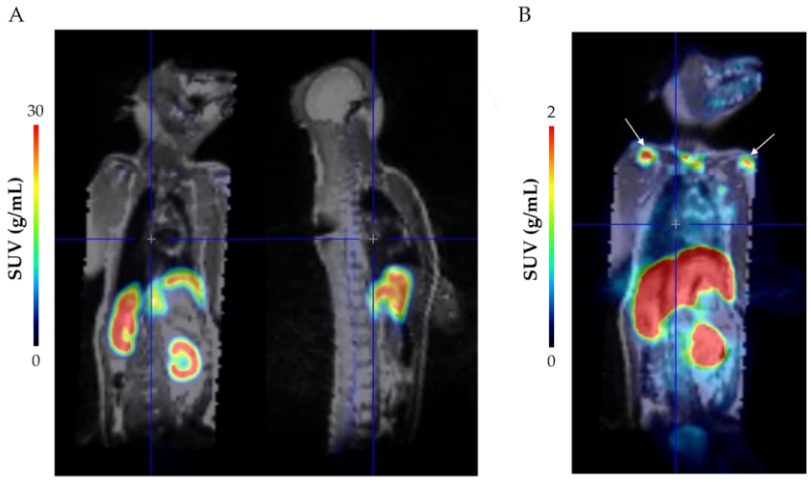

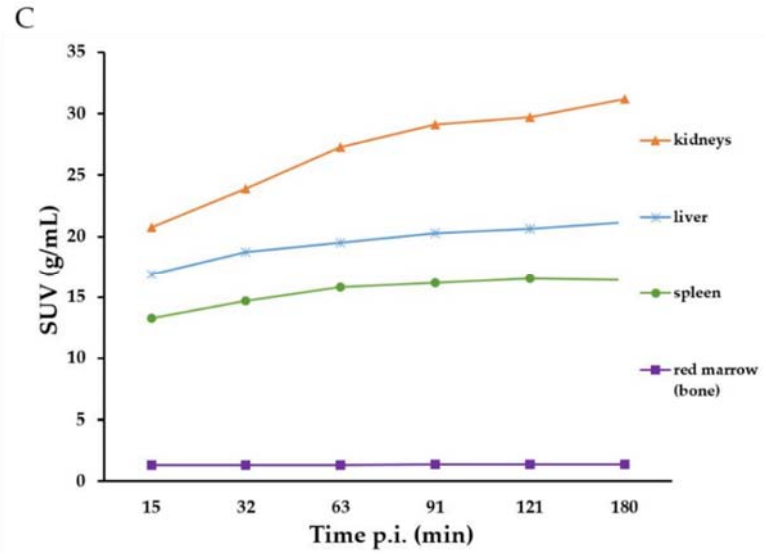


***Figure 6: Dynamic whole-body PET/magnetic resonance (MR) scan of [$^{18}$F]AlF-NOTA-2xDV1(c11sc12s) in a rhesus macaque (n = 1)*** *with the averaged maximum intensity projection (MIP) image (63 min p.i.) expressed as SUV (color scale) overlayed on the MR image (black/white) shown in (A). The MIP image (63 min p.i.) is shown in (B) with the red marrow (bone) highlighted with white arrows. TACs of kidneys, liver, spleen and red marrow (bone), expressed as SUV, have been added in (C).*

## 3. Conclusion

We succesfully designed a library of monomer and multimer constructs and evaluated their binding affinity for human and mouse CXCR4. The dimeric probe 2xDV1(c11sc12s) displayed an excellent *in vitro* profile in the non-radioactive competition assays and AlF-NOTA-2xDV1(c11sc12s) showed six-fold and four-fold higher affinity for human CXCR4 compared to Ga-Pentixafor and the first generation ligand AlF-NOTA-DV1-k-(DV3), respectively.

[$^{18}$F]AlF-NOTA-2xDV1(c11sc12s) was efficiently produced by an automated process with good RCY and RCP. The construct showed excellent *in vitro* and *in vivo* stability. *In vitro* radioligand binding assays showed CXCR4-specific uptake, however importantly, also non-CXCR4 specific uptake was observed.

In healthy mice, [$^{18}$F]AlF-NOTA-2xDV1(c11sc12s) displayed a strong uptake in mCXCR4-expressing organs, being the liver, spleen and bone marrow, as well as the kidneys, which is in line with the high *in vitro* affinity for mCXCR4. In the U87.hCXCR4 xenografted tumor mice only minor tumor uptake was observed, while the uptake in mCXCR4 expressing organs remained elevated and were only able to be fully blocked by co-injecting AMD3100 or 2xDV1(c11sc12s).

[$^{18}$F]AlF-NOTA-2xDV1(c11sc12s) exhibited a similar biodistribution in a non-human primate as in mice, with a high uptake in the liver and spleen. This was surprising, as in a clinical setting only limited uptake of [$^{68}$Ga]Pentixafor is observed in the liver and because the sequence homology between hCXCR4 and CXCR4 of a rhesus macaque is higher than between hCXCR4 and mCXCR4. The elevated

hepatic uptake suggests off-target binding of [$^{18}$F]AlF-NOTA-2xDV1(c11sc12s) in liver tissue, diminishing its clinical potential for human use.

In conclusion, the second generation D-peptide [$^{18}$F]AlF-NOTA-2xDV1(c11sc12s) does bind to CXCR4, however, the collected data suggest that there is at least one additional unidentified receptor involved in the binding of the radiotracer. Further improvement of the peptide structure to increase CXCR4 specificity will be required to enable CXCR4 specific imaging.

## 4. Materials and Methods

### 4.1. Synthesis of DV constructs

All the different DV probes, being DV1(c11a)-k-(DV3), DV1(c12a)-k-(DV3), DV1(c11ac12a)-k-(DV3), DV1(c11s)-k-(DV3), DV1(c12s)-k-(DV3), DV1(c11sc12s)-k-(DV3), 2xDV1(c11sc12s), 3xDV1(c11sc12s) and NOTA-2xDV1(c11sc12s), were purchased from Pepmic Co., Ltd (Suzhou, China) and analyzed by LC-HRMS. All compounds are >95% pure.The synthesis and characterization of the reference compound AlF-NOTA-2xDV1(c11sc12s) is described in SI.

### 4.2. [$^{18}$F]AlF radiolabeling of NOTA-2xDV1(c11sc12s):

The radiolabeling of the NOTA-construct was performed using a GMP compliant AllInOne® synthesis module (Trasis, Ans, Belgium) in a similar fashion, alike described by Tshibangu et al. [33].

Shortly, after irradiating the $^{18}$O enriched water target approx. 5 GBq [$^{18}$F] fluoride was trapped on a Sep-Pak light Accel plus anion exchange cartridge ($Cl^-$ form: Waters, Milford, Massachusetts, USA) and washed with 6 mL water (HPCE grade, Sigma Aldrich, Saint Louis, MO, USA). The cartridge was then eluted with a mixture of 250 µL NaCl 0.9% (99.999% trace metals basis NaCl (Sigma Aldrich) in HPCE grade water (Sigma Aldrich)) and 250 µL absolute ethanol and captured in a vial filled with 25 µL $AlCl_3$ 2mM. The mixture was allowed to react for 2 min under gentle nitrogen flow to form [$^{18}$F]AlF and subsequently mixed with the precursor solution, containing 100 nmoles NOTA-2xDV1(c11sc12s) and 0.95 mg/mL sodium ascorbate in sodium acetate 0.1 M pH 4.1/ absolute ethanol (40/60 *v/v*)). The mixture was heated to 100 °C for 10-20 min and after cooling down to 40 °C the crude was diluted with 15 mL formulation buffer, containing EtOH supplemented with NaAsc 0.59% dissolved in NaCl 0.9% in a 1.1/11.9 *v/v* ratio in water for injection.

After mixing under gentle nitrogen flow, the radiotracer was passed over a Sep-Pak light C18 cartridge (Waters), which was preconditioned with 5 mL absolute EtOH and 10 mL water. Non-chelated [$^{18}$F] fluoride species were removed by washing the cartridge with 20 mL formulation solution, followed by nitrogen. In the final step [$^{18}$F]AlF-NOTA-2xDV1(c11sc12s) was eluted from the cartridge with 1.6 mL $H_2O$/absolute ethanol mixture (60/40 *v/v*), followed by 17.4 mL formulation solution and nitrogen flushing through the cartridge, and sterile filtered using a 0.22 µm filter (Millex-GV, 0,22 µm, PVDF, 13 mm, Merck KGaA, Darmstadt, Germany). The activity of the final batch was measured using an ionization chamber (COMECER VIK-203, Comecer S.p.A., Castel Bolognese, Italy).

### 4.3. RadioHPLC

The radioHPLC system consisted of a degasser (Alltech Elite On-line degassing system, Grace Davison Discovery Sciences, Lokeren, Belgium), a pump (LaChrom Elite L-2130, Hitachi, Tokyo, Japan) coupled to a UV detector (L-2400, Hitachi, Tokyo, Japan), as well as to a three inch NaI(Tl) scintillation detector coupled to a GABI Star module, (Elysia Raytest Angleur, Belgium). The RCP was assessed using an Hamilton PRP-1 (1.5 µm, 4.1 × 150 mm) column (Hamilton, Bonaduz, Graubünden, Switzerland) eluted by a gradient composed of MilliQ water, as solvent A, and acetonitrile, as solvent B, both containing 0.1% trifluoroacetic acid, at a flow rate of 0.8 mL/min. During the 20 min gradient the following steps have been applied: 0 – 3.5 min, 95% A, 3.5 – 4.5 min 95% → 80% A, 4.5-5.5 min 80% → 70% A, 5.5 – 6.5 min 70% → 60% A, 6.5 – 10.0 min 60% → 50% A, 10.0 – 12.5 min 50% → 40% A, 12.5 min – 14.5 min 40% → 30% A, 14.5 – 17.0 min 30% → 15% A, 17.0 – 19.0 min 15% → 5% A, 19.0 -21.0 min 5% → 95% A [34].

### 4.4. [$^{68}$Ga]Ga radiolabeling of Pentixafor

PentixaFor was purchased from PentixaPharm GmbH (Würzburg, Germany) and was labelled using an automated SCINTOMCIS GRP module (SCINTOMICS GmbH, Fürstenfeldbruck, Germany) as described by Martin et al. [35].

### 4.5. *In vitro* assessment

#### 4.5.1. Cell culture conditions

The culture medium for human glioblastoma U87.MG cells was composed of Dulbecco's Modified Eagle Medium (DMEM) supplemented with 4 mM L-glutamine, 10% (v/v) fetal calf serum (Thermo Fisher Scientific, Waltham, MA, USA) and 0.01 M HEPES. The medium for U87.CD4 cells contained additional geneticin (0.2 mg/mL) (Thermo Fisher Scientific) and the medium for the U87.CD4.CXCR4, U87.CD4.CCR5, U87.CCR7 and U87.CD4.ACKR3 cell lines was further supplemented with puromycine (2 µg/mL) (Sigma-Aldrich). The Jurkat human T-cell leukemia cells overexpressing hCXCR4 were cultured in RPMI-1640 supplemented with 10% fetal bovine serum (FBS) and 2 mM glutamine. All the cells were cultured in a humidified incubator at 37°C and 5% $CO_2$.

#### 4.5.2. Animal welfare

The naïve biodistribution has been conducted in four weeks old female NRMI mice (Envigo RMS BV, Venray, The Netherlands), whereas the tumor model used four week old female SCID mice (CB17.Cg-PrkdcscidLystbg-J/Crl, Charles River Laboratories, Sulzfeld, Germany). The animals were housed in individually ventilated cages with temperature and humidity monitoring. Water and food access was displayed *ad libitum* and the light-dark cycle consisted of twelve hours. All animal experiments were approved by the KU Leuven ethical review board (reference P058/2020 (mice studies) and P112/2019 (non-human primate study)), and were carried out in accordance with Directive 2010/63/EU [36].

#### 4.5.3.hCXCR4/mCXCR4 affinity assessment

The affinity ($IC_{50}$) towards mCXCR4 or hCXCR4 was assessed as described by Schoofs et al. [37]. Briefly, compounds were diluted in a 96-well plate (100 µL/well, in assay buffer). Assay buffer was composed of 20mM HEPES (Thermo Fisher Scientific) and 0.2% BSA (Sigma-Aldrich) dissolved in Hank's Balanced Salt Solution (Thermo Fisher Scientific) at pH 7.4. Then 50 µL containing $0.25*10^6$ U87.mCXCR4 or Jurkat.hCXCR4 cells were added to each well and left to incubate for 15min at room temperature. Finally, 50 µL of murine or human (100 ng/mL) $CXCL12^{AF647}$ (Almac, Craigavon, United Kingdom) was added, respectively, and the plate was left to incubate for 30 min at room temperature in the dark. Compound-free control samples with or without $CXCL12^{AF647}$ were included as described [37]. After incubation, cells were washed twice and finally fixed in 1% paraformaldehyde (Merck) before being analyzed by flow cytometry. $IC_{50}$ values were calculated by applying nonlinear regression in GraphPad Prism 9 (Graph Pad Software, San Diego, CA, USA).

#### 4.5.4. *In vitro* radioligand cell binding and internalization assay

The binding assays were conducted on $0.2*10^6$ hCXCR4-expressing U87.CXCR4 cells or on U87.MG, U87.CD4, U87.CD4.CXCR4, U87.CD4.CCR5, U87.CD4.CCR7 or U87.CD4.ACKR3 cells, which were plated one day prior. The overexpression of the specific receptor and absence of any other receptors of the CXCR family has been confirmed via flow cytomery [25]. On the day of the assay, the medium was removed and approx. 150 kBq radiotracer was added onto each well, while being diluted in assay buffer, containing 20 mM HEPES (Thermo Fisher Scientific) and 0.2% BSA (Sigma-Aldrich) in Hank's Balanced Salt Solution (Thermo Fisher Scientific) at pH 7.4. For blocking studies, the corresponding competitor (100 or 75 µM) was added simultaneously with the radiotracer, namely 4,4′-diisothiocyanatostilbene-2,2′-disulfonic acid (Sigma-Aldrich), AMD3100 (Sigma-Aldrich), Maraviroc (MedChemExpress, Monmouth Junction, NJ, USA), VUF11207 (Laboratory of Virology and Chemotherapy, KU Leuven, Belgium), or (2x)DV1(c11sc12s) as self-block. No CCR7 competitor was used, since no potent or selective CCR7 antagonist has been described [26]. The incubation was performed at 37°C or 4°C for 1h. After removing the medium, the cells were washed with 600 µL ice cold PBS. These fractions were collected and named the “non-bound” fraction. This was followed by washing the cells twice for 5 min with 600 µL ice cold glycine.HCl buffer (50 mM, pH 2.8). The collected fractions were called the “membrane-bound” fraction. Then 500 µL of solvent A100 (Chemometec, Allerod, Denmark) and 500 µL of reagent B (Chemometec) were added to lyse the cells, followed by a wash with 500 µL PBS. The collected fractions were named the “internalized” fraction. Thereupon, radioactivity in every fraction was counted in a gamma counter (Perkin-Elmer, Wizard2 2480, Waltham, MA, USA) and the number of cells was counted using a NucleoCounter® NC-100™ (Chemometec). The membrane and internalized fraction was corrected to $0.2*10^6$ cells. Every experiment has been performed in triplicate.

### 4.6. *In vivo* assessment

#### 4.6.1. Preparation of U87.CXCR4 tumor model

The U87.CXCR4 tumor model was used as described in Fridman et al. [38]. Briefly, $1x10^6$ U87.hCXCR4 cells were suspended in a 1:1 ratio using Cultrex Basement Membrane Extract (R&D systems, Minneapolis, MN, USA) and inoculated on the right shoulder of four weeks old female SCID mice (CB17.Cg-PrkdcscidLystbg-J/Crl; Charles River Laboratories, Sulzfeld, Germany). The tumor size was measured every second day using a Vernier caliper and calculated using the h × l × w formula. As soon as the tumors reached the size of 200 $mm^3$, the mice were randomly distributed into the different cohorts for the subsequent biodistribution study. The tumor model with xenografted U87.CXCR4 tumors has been validated using [$^{68}$Ga]Pentixafor [16].

#### 4.6.2. PET/CT imaging and biodistribution in wild-type mice and U87.CXCR4 xenografted tumor mice

Female NMRI mice or U87.hCXCR4 tumor-bearing mice were anesthetized (2.5% isoflurane in $O_2$ at 1 L/min flow rate) and injected i.v. with [$^{18}$F]AlF-NOTA-2xDV1(c11sc12s) (1.5–3.0 MBq/0.2─0.4 nmol NOTA-2xDV1(c11sc12s)/mouse, n = 4 (NMRI), n = 8 (U87.hCXCR4), in the presence or absence of AMD3100 (5 mg/kg, n=1 (NMRI), n = 4 (U87.hCXCR4)), AMD070 (5 mg/kg, n = 4 (U87.hCXCR4)) or 2xDV1(c11sc12s) (U87.hCXCR4, 15 nmoles (n = 3)). The displacement study was conducted by injecting AMD3100 i.v. (5 mg/kg, n = 4) 15 min post radiotracer injection. Dynamic PET images were acquired for 60 min immediately after intravenous injection using a beta-cube PET scanner (Molecubes, Ghent, Belgium). The mice were kept under gas anesthesia during the entire procedure (2.5% isoflurane in $O_2$ at 1 L/min flow rate), with temperature and respiration monitored throughout. After PET scanning, a CT image was acquired for anatomic coregistration with an X-cube CT scanner (Molecubes), using the 'general' protocol with the following parameters: 50kVp, 480 exposures, 85 ms/projection, 100 μA tube current, rotation time 60 s. After scanning, mice were sacrificed 75 min p.i. and a whole-body biodistribution study was performed. Blood and major organs were collected in tared tubes and weighed. Quantification of radioactivity in blood, organs, and other body parts was performed using an automated gamma counter equipped with a 3-inch NaI(Tl) well crystal coupled to a multichannel analyzer, mounted in a sample changer (Perkin Elmer 1480 Wizard 3q). Counts were corrected for background radiation, physical decay and counter dead time. The values have been expressed in standardized uptake values ((SUV; tissue activity concentration (MBq/g)/[injected activity (MBq)/body weight (g)])) or percentage of injected dose ((%ID; tissue activity (MBq)/injected activity (MBq))).

#### 4.6.3. Radiometabolite study in mice and rhesus macaque

The *in vivo* stability has been assessed by collecting whole blood in EDTA tubes (Greiner Bio-One $K_2$EDTA MiniCollect tubes) 15 min (n = 3) or 75 min (n = 3) p.i. from wild-type mice and centrifuging it for 5 min at 3000 × *g*. The plasma fraction was then diluted in a 1:2 ratio with acetonitrile and

centrifuged for 5 min at 3000 × *g*. After collecting the supernatant, the fraction was diluted in a 1:10 ratio with MQ water and passed through a 0.22 µm Millex-GV Filter (Merck KGaA). In addition, urine samples were collected 75 min (n = 3) p.i. by pushing onto the bladder and filtered (0.22 µm Millex-GV Filter) as well prior to injection onto the column. The same procedure was applied with the rhesus macaque, however, the whole blood sampling was performed at 10, 30 and 60 min p.i. via the vena saphena and urine was collected 180 min p.i.. The resulted chromatograms have been added in the SI.

#### 4.6.4. PET/MR imaging in a non-human primate

The rhesus monkey (*Macaca mulatta*, male, 5 years old, 7.95 kg) was sedated with an intramuscular injection of 0.25 mL ketamine hydrochloride (100 mg/mL, Nimatek®) and 0.5 mL medetomidine hydrochloride (1 mg/mL, Domitor®) ~ 75 min prior to the initiation of PET scans and transported to the PET facility. Sixty minutes after the first injection, and from then on every 30 min, the rhesus monkey received an additional dose of 0.125 ml ketamine hydrochloride and 0.25 ml medetomidine hydrochloride via i.v. injection. The $O_2$ and $CO_2$ saturation in the blood and the heartbeat were constantly monitored. Temperature was regulated via a heating pad. The breathing frequency and the eye response were checked by the lab technician regularly. 183 MBq (24.4 nmoles) [$^{18}$F]AlF-NOTA-2xDV1(c11sc12s) was injected i.v. and i*n vivo* pharmacokinetics were determined by whole-body PET/magnetic resonance (MR) imaging of the tracer distribution up to 3 hours after tracer injection. Blood was collected via venous blood sampling (vena saphena) at 10, 30 and 60 min p.i.. Plasma metabolites were determined by radioHPLC (procedure described above). After scanning (180 min p.i.), urine was collected by gently pressing the bladder and urine metabolites were determined by radioHPLC (procedure described above).

### 4.7. Image processing and analysis for mice

PET data were histogrammed into 14 frames (4 × 15 s, 4 × 1 min, 1 × 5 min, 5 × 10 min) and reconstructed into a 192 × 192 image matrix with 0.4 mm voxels using 30 iterations using the native Maximum-Likelihood Expectation-Maximization (MLEM) algorithm with corrections for randoms, scatter, attenuation and decay. CT data were reconstructed using a regularized statistical (iterative) image reconstruction algorithm using non-negative least squares, using an isotropic 200 µm voxel size and scaled to Hounsfield Units (HUs) after calibration against a standard air/water phantom [39]. Using PFUS v4.0 to display the fused PET-CT image (PMOD Technologies GmbH, Zürich, Switzerland), volumes of interest were manually drawn over the tumor while a sphere of 3 mm diameter was placed over the left lobe of the liver. Radiotracer uptake at 60 min, expressed as $SUV_{mean}$, was the outcome measure.

### 4.8. Image Processing and analysis for non-human primate

PET data were collected in list mode and corrected for randoms, scatter and deadtime. Attenuation correction was performed. Whole-body PET scans were acquired at 15, 32, 63, 91, 121 and 180 min after tracer injection. For each whole-body scan, a LAVA-Flex sequence (GE proprietary DIXON sequence, MP26) was acquired to generate the MR based attenuation map, by measuring the in-phase (water and fat) and out-of-phase (water minus fat) T1-weighted signal. Next, water and fat tissue were segmented and assigned the appropriate attenuation factors. In addition, a model-based lung segmentation was performed to assign the appropriate attenuation factor to lung tissue while for the head, the skull bone was included using an atlas-based approach. Ordered Subsets Expectation Maximization (28 subsets with 4 iterations), including time-of-flight information, resolution modeling, and Gaussian post smoothing with a Full-Width-at-Half-Maximum (FWHM) kernel of 4.5 mm (isotropic), was used for reconstruction.

All source organs with relevant detectable activity were delineated on the PET images with MR-AC map as guidance using PMOD version 4.1. Time-integrated activity coefficients (normalized cumulated activity; NCA) were calculated for each source organ by integrating their time-activity curves through curve fitting and normalizing the cumulated activity to the injected activity.

Image analysis was performed using PMOD version 4.1. VOIs were drawn over organs of interest on the PET image and SUVmean in these VOIs were determined.

### 4.9. Statistical analysis

The results are reported as mean ± standard deviation (SD). Statistical significance has been defined as $p < 0.05$ and was calculated using independent-samples t-test on Microsoft Excel.

**Acknowledgments**

The authors would like to thank Julie Cornelis, Christopher Cawthorne, Cindy Heens, Christophe Ulens and Geert Schoofs for technical support and insights during the *in vitro* and *in vivo* assays.

**Funding:** This research received support from Stichting tegen kanker ("Peptide based CXCR4-targeting for PET imaging and radionuclide therapy", C/2020/1528) and internal funding KU Leuven. C.M.D is a Senior Clinical Investigator at the FWO. The PET-CT equipment was funded via an FWO medium infrastructure grant (AKUL15-30/G0H1216N).

[1] S. Chatterjee, B. Behnam Azad, and S. Nimmagadda, "The intricate role of CXCR4 in cancer.," *Adv. Cancer Res.*, vol. 124, pp. 31–82, 2014, doi: 10.1016/B978-0-12-411638-2.00002-1.

[2] E. Gourni *et al.*, "PET of CXCR4 expression by a (68)Ga-labeled highly specific targeted contrast agent," *J Nucl Med*, vol. 52, no. 11. pp. 1803–10, 2011. doi: 10.2967/jnumed.111.098798.

[3] A. Poschenrieder *et al.*, "First (18)F-Labeled Pentixafor-Based Imaging Agent for PET Imaging of CXCR4 Expression In Vivo.," *Tomogr. Ann Arbor Mich*, vol. 2, no. 2, pp. 85–93, Jun. 2016, doi: 10.18383/j.tom.2016.00130.

[4] H. Hänscheid *et al.*, "Biokinetics and Dosimetry of [ 177 Lu]Lu-Pentixather," *J Nucl Med*, vol. 63, no. 5. pp. 754–760, 2022. doi: 10.2967/jnumed.121.262295.
[5] K. Herrmann *et al.*, "First-in-Human Experience of CXCR4-Directed Endoradiotherapy with 177Lu- and 90Y-Labeled Pentixather in Advanced-Stage Multiple Myeloma with Extensive Intra- and Extramedullary Disease.," *J. Nucl. Med. Off. Publ. Soc. Nucl. Med.*, vol. 57, no. 2, pp. 248–251, Feb. 2016, doi: 10.2967/jnumed.115.167361.
[6] A. Sanchez-Crespo, "Comparison of Gallium-68 and Fluorine-18 imaging characteristics in positron emission tomography.," *Appl. Radiat. Isot. Data Instrum. Methods Use Agric. Ind. Med.*, vol. 76, pp. 55–62, Jun. 2013, doi: 10.1016/j.apradiso.2012.06.034.
[7] Hannes Leupe *et al.*, "$^{18}$F-Labeled Somatostatin Analogs as PET Tracers for the Somatostatin Receptor: Ready for Clinical Use," *J. Nucl. Med.*, p. 265622, May 2023, doi: 10.2967/jnumed.123.265622.
[8] K. S. Pedersen, K. M. Nielsen, J. Fonslet, M. Jensen, and F. Zhuravlev, "Separation of Radiogallium from Zinc Using Membrane-Based Liquid-Liquid Extraction in Flow: Experimental and COSMO-RS Studies," *Solvent Extraction and Ion Exchange*, vol. 37, no. 5. pp. 376–391, 2021. doi: 10.1080/07366299.2019.1646982.
[9] C. Lapa *et al.*, "CXCR4-directed endoradiotherapy induces high response rates in extramedullary relapsed Multiple Myeloma.," *Theranostics*, vol. 7, no. 6, pp. 1589–1597, 2017, doi: 10.7150/thno.19050.
[10] M. Schottelius *et al.*, "[(177)Lu]pentixather: Comprehensive Preclinical Characterization of a First CXCR4-directed Endoradiotherapeutic Agent," *Theranostics*, vol. 7, no. 9. pp. 2350–2362, 2017. doi: 10.7150/thno.19119.
[11] T. N. Kledal *et al.*, "A Broad-Spectrum Chemokine Antagonist Encoded by Kaposi's Sarcoma-Associated Herpesvirus," *Science*, vol. 277, no. 5332, pp. 1656–1659, Sep. 1997, doi: 10.1126/science.277.5332.1656.
[12] N. Zhou *et al.*, "Exploring the Stereochemistry of CXCR4-Peptide Recognition and Inhibiting HIV-1 Entry with d-Peptides Derived from Chemokines*," *J. Biol. Chem.*, vol. 277, no. 20, pp. 17476–17485, May 2002, doi: 10.1074/jbc.M202063200.
[13] L. Qin *et al.*, "Structural biology. Crystal structure of the chemokine receptor CXCR4 in complex with a viral chemokine," *Science*, vol. 347, no. 6226. pp. 1117–22, 2015. doi: 10.1126/science.1261064.
[14] I. Heon Lee, M. S. Palombo, X. Zhang, Z. Szekely, and P. J. Sinko, "Design and evaluation of a CXCR4 targeting peptide 4DV3 as an HIV entry inhibitor and a ligand for targeted drug delivery," *Eur J Pharm Biopharm*, vol. 138. pp. 11–22, 2019. doi: 10.1016/j.ejpb.2018.06.004.
[15] Y. Xu, S. Duggineni, S. Espitia, D. D. Richman, J. An, and Z. Huang, "A synthetic bivalent ligand of CXCR4 inhibits HIV infection.," *Biochem. Biophys. Res. Commun.*, vol. 435, no. 4, pp. 646–650, Jun. 2013, doi: 10.1016/j.bbrc.2013.05.038.
[16] K. Luyten *et al.*, "D-Peptide-Based Probe for CXCR4-Targeted Molecular Imaging and Radionuclide Therapy," *Pharmaceutics*, vol. 13, no. 10. 2021. doi: 10.3390/pharmaceutics13101619.
[17] W. T. Choi *et al.*, "A novel synthetic bivalent ligand to probe chemokine receptor CXCR4 dimerization and inhibit HIV-1 entry," *Biochemistry*, vol. 51, no. 36. pp. 7078–86, 2012. doi: 10.1021/bi2016712.
[18] E. Coudert *et al.*, "Annotation of biologically relevant ligands in UniProtKB using ChEBI," *Bioinformatics*, vol. 39, no. 1. 2023. doi: 10.1093/bioinformatics/btac793.
[19] S. Jähnichen *et al.*, "CXCR4 nanobodies (VHH-based single variable domains) potently inhibit chemotaxis and HIV-1 replication and mobilize stem cells," *Proc Natl Acad Sci U S A*, vol. 107, no. 47. pp. 20565–70, 2010. doi: 10.1073/pnas.1012865107.
[20] D. Uchida *et al.*, "Effect of a novel orally bioavailable CXCR4 inhibitor, AMD070, on the metastasis of oral cancer cells.," *Oncol. Rep.*, vol. 40, no. 1, pp. 303–308, Jul. 2018, doi: 10.3892/or.2018.6400.
[21] A. S. Jørgensen *et al.*, "Biased action of the CXCR4-targeting drug plerixafor is essential for its superior hematopoietic stem cell mobilization.," *Commun. Biol.*, vol. 4, no. 1, p. 569, May 2021, doi: 10.1038/s42003-021-02070-9.

[22] M. M. Rosenkilde, L.-O. Gerlach, J. S. Jakobsen, R. T. Skerlj, G. J. Bridger, and T. W. Schwartz, "Molecular mechanism of AMD3100 antagonism in the CXCR4 receptor: transfer of binding site to the CXCR3 receptor.," *J. Biol. Chem.*, vol. 279, no. 4, pp. 3033–3041, Jan. 2004, doi: 10.1074/jbc.M309546200.
[23] R. S. Y. Wong, V. Bodart, M. Metz, J. Labrecque, G. Bridger, and S. P. Fricker, "Comparison of the potential multiple binding modes of bicyclam, monocylam, and noncyclam small-molecule CXC chemokine receptor 4 inhibitors.," *Mol. Pharmacol.*, vol. 74, no. 6, pp. 1485–1495, Dec. 2008, doi: 10.1124/mol.108.049775.
[24] M. A. C. Neves, S. Simões, and M. L. Sá e Melo, "Ligand-guided optimization of CXCR4 homology models for virtual screening using a multiple chemotype approach.," *J. Comput. Aided Mol. Des.*, vol. 24, no. 12, pp. 1023–1033, Dec. 2010, doi: 10.1007/s10822-010-9393-x.
[25] M. Rose *et al.*, "Surfaceome Proteomic of Glioblastoma Revealed Potential Targets for Immunotherapy," *Front Immunol*, vol. 12. p. 746168, 2021. doi: 10.3389/fimmu.2021.746168.
[26] S. Hatse, K. Princen, G. Bridger, E. De Clercq, and D. Schols, "Chemokine receptor inhibition by AMD3100 is strictly confined to CXCR4," *FEBS Lett*, vol. 527, no. 1–3. pp. 255–62, 2002. doi: 10.1016/s0014-5793(02)03143-5.
[27] I. Kalatskaya, Y. A. Berchiche, S. Gravel, B. J. Limberg, J. S. Rosenbaum, and N. Heveker, "AMD3100 Is a CXCR7 Ligand with Allosteric Agonist Properties," *Molecular Pharmacology*, vol. 75, no. 5. p. 1240, 2009. doi: 10.1124/mol.108.053389.
[28] S. Gravel *et al.*, "The peptidomimetic CXCR4 antagonist TC14012 recruits beta-arrestin to CXCR7: roles of receptor domains," *J Biol Chem*, vol. 285, no. 49. pp. 37939–43, 2010. doi: 10.1074/jbc.C110.147470.
[29] Y. Yuan *et al.*, "A Bivalent Ligand Targeting the Putative Mu Opioid Receptor and Chemokine Receptor CCR5 Heterodimers: Binding Affinity versus Functional Activities," *Medchemcomm*, vol. 4, no. 5. pp. 847–851, 2013. doi: 10.1039/C3MD00080J.
[30] M. Wijtmans *et al.*, "Synthesis, modeling and functional activity of substituted styrene-amides as small-molecule CXCR7 agonists," *Eur J Med Chem*, vol. 51. pp. 184–92, 2012. doi: 10.1016/j.ejmech.2012.02.041.
[31] H. J. Wester *et al.*, "Disclosing the CXCR4 expression in lymphoproliferative diseases by targeted molecular imaging.," *Theranostics*, vol. 5, no. 6, pp. 618–630, 2015, doi: 10.7150/thno.11251.
[32] M. Soave *et al.*, "Monitoring Allosteric Interactions with CXCR4 Using NanoBiT Conjugated Nanobodies.," *Cell Chem. Biol.*, vol. 27, no. 10, pp. 1250-1261.e5, Oct. 2020, doi: 10.1016/j.chembiol.2020.06.006.
[33] T. Tshibangu *et al.*, "Automated GMP compliant production of [," *EJNMMI Radiopharm Chem*, vol. 5, no. 1. p. 4, 2020. doi: 10.1186/s41181-019-0084-1.
[34] D. Ory *et al.*, "Retention of [(18)F]fluoride on reversed phase HPLC columns," *J Pharm Biomed Anal*, vol. 111. pp. 209–14, 2015. doi: 10.1016/j.jpba.2015.04.009.
[35] R. Martin, S. Jüttler, M. Müller, and H. J. Wester, "Cationic eluate pretreatment for automated synthesis of [$^{68}$Ga]CPCR4.2," *Nucl Med Biol*, vol. 41, no. 1. pp. 84–9, 2014. doi: 10.1016/j.nucmedbio.2013.09.002.
[36] N. Percie du Sert *et al.*, "The ARRIVE guidelines 2.0: Updated guidelines for reporting animal research.," *PLoS Biol.*, vol. 18, no. 7, p. e3000410, Jul. 2020, doi: 10.1371/journal.pbio.3000410.
[37] G. Schoofs, A. Van Hout, T. D'huys, D. Schols, and T. Van Loy, "A Flow Cytometry-based Assay to Identify Compounds That Disrupt Binding of Fluorescently-labeled CXC Chemokine Ligand 12 to CXC Chemokine Receptor 4," *J Vis Exp*, no. 133. 2018. doi: 10.3791/57271.
[38] R. Fridman, G. Benton, I. Aranoutova, H. K. Kleinman, and R. D. Bonfil, "Increased initiation and growth of tumor cell lines, cancer stem cells and biopsy material in mice using basement membrane matrix protein (Cultrex or Matrigel) co-injection," *Nat. Protoc.*, vol. 7, no. 6, pp. 1138–1144, Jun. 2012, doi: 10.1038/nprot.2012.053.
[39] B. Vandeghinste *et al.*, "Iterative CT Reconstruction Using Shearlet-Based Regularization," *IEEE Trans. Nucl. Sci.*, vol. 60, no. 5, pp. 3305–3317, Oct. 2013, doi: 10.1109/TNS.2013.2275994.